Supporting Information

Modulating d-band center of boron doped single-atom site to boost oxygen reduction reaction

He Sun,[‡a] Mengfan Wang,[‡b] Xinchuan Du,[‡a] Yu Jiao,[c] Sisi Liu,[b] Tao Qian,[b] Yichao Yan,[a] Chen Liu,[d] Min Liao,[*d] Qinghua Zhang,[e] Linxing Meng,[b] Lin Gu,[e] Jie Xiong,[*a] Chenglin Yan[*b]

[a] State Key Laboratory of Electronic Thin Films and Integrated Devices, University of Electronic Science and Technology of China, Chengdu 610054, PR China

E-mail: jiexiong@uestc.edu.cn

[b] College of Energy, Key Laboratory of Advanced Carbon Materials and Wearable Energy Technologies of Jiangsu Province, Key Lab of Advanced Optical Manufacturing Technologies of Jiangsu Province & Key Lab of Modern Optical Technologies of Education Ministry of China, Soochow University, Suzhou 215006, PR China

E-mail: email: c.yan@suda.edu.cn

[c] School of Applied and Chemical Engineering, Xichang College, Xichang 615053, P. R. China

[d] Hunan Provincial Key Laboratory of Thin Film Materials and Devices, School of Materials Science and Engineering, Xiangtan University, Xiangtan 411105, PR China

E-mail: mliao@xtu.edu.cn

[e] Beijing National Laboratory for Condensed Matter Physics, Institute of Physics, Chinese Academy of Science, Beijing 100190, PR China

† Electronic supplementary information (ESI) available.

‡ These authors contributed equally.

1. Sample preparation

Synthesis of Fe$_{SA}$/B,N-CNT, Fe$_{SA}$/N-CNT, Fe$_{NP}$/N-CNT and N doped carbon

Typically, polyvinylpyrrolidone (4 g), zinc nitrate (0.42 g), and 2-methylimidazole (3.36 g) were dissolved in 40 ml deionized water in a glass vial. The mixture was stirred at room temperature for 3 h. After adding ferric chloride (40 mg) into the solution, The vial was capped and 120 °C oven for 12 h. Lyophilization was performed to dry the mixture. 100 mg of the obtained powder and 250 mg of sodium borohydride were placed at two separate positions in a ceramic crucible with the sodium borohydride at the upstream side. The samples were heated at 900 °C for 2 h under argon atomsphere. The pyrolysis products were acid-washed with 1 M HCl solution at 80 °C ovenight and then filtered and washed with plenty of deionized water. The final catalysts were obtained by vacuum drying. For comparsion, the Fe$_{SA}$/N-CNT was synthesized following the same procedure as Fe$_{SA}$/B,N-CNT, but without involving sodium borohydride in the pyrolysis process. Fe$_{NP}$/N-CNT was synthesized following the same procedure as Fe$_{SA}$/N-CNT, except for the addition of 240 mg ferric chloride. The N doped carbon was synthesized following the same procedure as Fe$_{SA}$/N-CNT, except for the addition of ammonium persulphate (100 mg) instead of ferric chloride.

2. Sample characterization

The morphologies were observed with a field emission scanning electron microscope (FESEM, SU8010, Japan) and a field emission transmission electron microscope (FETEM, Tecnai G2 F20, Hong Kong). The dispersion of single Fe atoms was characterized by atomic-resolution high-angle annular dark-field scanning transmission electron microscopy (HAADF-STEM) on a JEOL JEM-ARM200F instrument equipped with probe spherical aberration corrector. The iron concentrations of the samples were conducted on the inductively coupled plasma atomic emission spectroscopy (ICP-OES). Surface elemental analysis was performed on XPS (Kratos Axis Ultra Dld, Japan). The X-ray absorption find structure spectra (Fe K-edge) were collected at 1W1B station in Beijing Synchrotron Radiation Facility (BSRF). The storage rings of BSRF was operated at 2.5 GeV with a maximum current of 250 mA. Using Si (111) double-crystal monochromator, the data collection was carried out

in transmission mode using ionization chamber for Fe foil and in fluorescence excitation mode using a Lytle detector for Fe_{SA}/B,N-CNT. All spectra were collected in ambient conditions. The composition of the catalysts was characterized by X-ray diffraction pattern (XRD, D8 Advance, Bruker) and Raman spectroscopy (HR evolution, Horiba Jobin Yvon, France). N_2-sorption analysis was performed by an ASAP 2020 accelerated surface area and porosimetry instrument (Micromeritics), equipped with automated surface area, at 77 K using BET calculations for the surface area.

3. Electrochemical measurements

All electrochemical measurements were carried out in a conventional three-electrode system using WaveDriver 20 bipotentiostat (Pine Instrument Company, USA). A Rotating Disk Electrode (RDE) with a glassy carbon disk served as the substrate was used as the working electrode, a Ag/AgCl and carbon rod were used as reference and counter electrode. The catalyst ink was prepared by dispersing 2 mg catalysts and 0.5 mg Acetylene Black in 380 μL ethanol and 20 μL Nafion solution (5 wt%) in an ultrasonic bath for at least 30 min. 8 μL of catalyst ink was then coated on glassy carbon disk. For comparison, Commercial Pt/C (20 wt%, Johnson Matthey) catalyst ink was prepared by dispersing 1 mg catalysts in 250 μL ethanol and 10 μL Nafion solution (5 wt%). 10 μL of catalyst ink was then coated on glassy carbon disk. The electrolyte was 0.1 M KOH. Before each experiment, electrolyte was saturated with N_2/O_2 by gassing with N_2/O_2 for at least 30 min. CV tests were performed in N_2- and O_2-saturated alkaline solution at 50 mV s^{-1}. LSV tests were performed in O_2-saturated alkaline solution at 400, 625, 900, 1,225, 1,600, 2,025, 2,500 rpm with a scan rate of 10 mV s^{-1}. Unless noted otherwise, all the potentials mentioned in this paper were versus RHE. RRDE tests were conducted in O_2-saturated 0.1 M KOH solution with the scan rate of 10 mV s^{-1} under the rotation rate of 1,600 rpm. For the analysis of peroxide yield, the ring potential was held constant at 1.2 V vs. RHE. The percent of H_2O_2 , the number of electron transfer (n) and kinetic current density (J_k) were determined by the following Koutecky–Levich equations:

$$\% \ (H_2O_2) = 200 \frac{I_r/N}{I_d + I_r/N}$$

(1)

$$n = 4\frac{I_d}{I_d + I_r/N} \tag{2}$$

$$\frac{1}{J} = \frac{1}{J_L} + \frac{1}{J_k} \tag{3}$$

$$J_k = nFkC_0 \tag{4}$$

where I_d is the disk current, I_r is the ring current, and N (= 0.37) is the current collection efficiency of the Pt ring, J is the measured current density, J_L and J_K are the limiting and kinetic current densities. n is the overall number of electrons transferred in oxygen reduction, F is the Faraday constant (F=96485 C mol^{-1}), C_0 is the bulk concentration of O_2, k is the electron-transfer rate constant.

The possible crossover effect caused by methanol was examined upon adding 3 M methanol into 0.1 M KOH electrolyte using the i-t technique. The durability of different samples were measured via chronoamperometric measurements in 0.1 M KOH with a rotation speed of 1,600 rpm.

Tafel slopes were obtained according to the Tafel equation:

$$\eta = a + b \log j \tag{5}$$

where η was the overpotential, j was the measured current density, and b was the Tafel slope. The electrochemical impedance spectroscopy (EIS) measurements were carried out in a frequency range of 0.01 Hz-100 KHz. The durability of different samples were measured via chronoamperometric measurements at 1,600 rpm in 0.1 M KOH.

The electrochemical surface areas (ECSA) values of different catalysts were determined by measuring the capacitive current associated with double-layer charging from the scan-rate dependence of CVs. The ECSA was measured on the same working electrode and electrolyte (0.1 M KOH). The potential window of CVs was 1.10–1.15 V vs. RHE, and the scan rates were 2, 4, 6, 8, and 10 mV/s. The double layer capacitance (C_{dl}) was estimated by plotting the current density at 1.14V vs. RHE against the scan rate. The slope is twice of C_{dl}.

4. Simulation methods and computational modeling

4.1 Computational method.

The spin-polarized first-principle calculations were performed using the all-electron code Fritz-Haber Institute ab-initio molecules simulations package (FHI-aims).[1] The exchange-correlation potentials were treated by the generalized gradient approximation (GGA) developed by Perdew, Burke, and Ernzerhof (PBE).[2, 3] The current work employs the armchair (6, 6) single-walled carbon nanotube (CNT). At least 10 Å of vacuum layer are exposed to the direction perpendicular to the CNT axis. The B-doped FeN_4/CNT supercell has a hexagonal lattice with x, y = 20.00 Å and z = 14.76 Å. The Brillion zone was sampled by an appropriate Γ-centered Monkhorst-Pack grid with a density of at least 0.03 $Å^{-1}$.[4] All geometrical structures were fully relaxed to its ground state until the charge density and the total energy were below of 10^{-4} $eV/Å^3$ and 10^{-5} eV, respectively. To account for the weak van der Waals interaction, the functionals were augmented by the Tkatchenko and Scheffler scheme.[5, 6]

4.2 Formation energy

We compared formation energies of various possible models. Single B dopant could be generally classified into three different types, depending on the local chemical environment of carbon in the system: isolated B far away from FeN_4 moiety (B_{iso}), B in a pentatomic ring bonded with FeN_4 moiety (B_{pen}), B in a hexatomic ring bonded with FeN^4 moiety (B_{hex}). With increasing B doping concentration, the situation of double B dopants incorporation of "Fe-porphyrin" into CNTs had been considered, affecting on the catalytic activity and electrical conducting of the system: two adjacent B dopants in a pentatomic or hexatomic ring (B_2-adj-pen, B_2-adj-hex), two opposite B dopants in different pentatomic or hexatomic rings (B_2-opp-pen, B_2-opp-hex), two adjacent B dopants bonded with the same N (B_2-adj-N) and two interval B dopants in different rings (B_2-pen-hex).

The formation energy (E_f) [7] of various B-doped FeN_4/CNTs are calculated for comparing the relative stability of different B doped FeN_4/CNT systems by the equation of

$$E_f = E_{tot}(B_C) - E_{tot} + \sum_i n_i \mu_i \qquad (6)$$

where, $E_{tot}(B_C)$ was the total energy of the supercell containing B substitutional carbon defects, E_{tot} was the total energy of the supercell without defects, n_i standed for the number of constituent element i being added/removed from the FeN$_4$/CNT supercell, μ_i referred to the atomic chemical potential, E_{VBM} represented the valence band maximum (VBM) energy of the perfect supercell, E_F meant the Fermi energy measured from the VBM, varying in the range of the band gap (E_g), and ΔV was the potential difference between the doped system and FeN$_4$/CNT supercell.

4.3 Gibbs free energy of each ORR steps

In alkaline media the overall ORR could be expressed as:

$$2H_2O + O_2 + 4e^- \rightarrow 4OH^- \qquad (7)$$

Since the ORR on FeN$_4$/CNT proceeded mainly along four-electron processes, we thus explored the reaction via four-electron pathways. The elementary reaction steps were listed as below:

$$H_2O + O_2 + e^- \rightarrow HOO^* + OH^- \qquad (8)$$

$$HOO^* + e^- \rightarrow O^* + OH^- \qquad (9)$$

$$O^* + H_2O + e^- \rightarrow HO^* + OH^- \qquad (10)$$

$$HO^* + e^- \rightarrow * + OH^- \qquad (11)$$
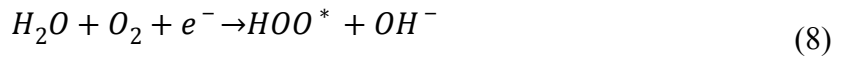
where * represented an adsorption site. To quantitatively access the activity of the B-doped systems, we calculated the adsorption energies of ORR intermediates following the approach of Nørskov et al:

$$\Delta E_{HOO*} = E_{HOO*} - E_* - \left[2E_{H_2O}(l) - 3/2E_{H_2}(g)\right]$$

$$\tag{12}$$

$$\Delta E_{HO*} = E_{HO*} - E_* - \left[E_{H_2O}(l) - 1/2E_{H_2}(g)\right] \tag{13}$$

$$\Delta E_{O*} = E_{O*} - E_* - \left[E_{H_2O} - E_{H_2}\right] \tag{14}$$

where, for example, E_{O*} denoted the total energy of an oxygen atom adsorbed on the catalyst obtained by the calculations, H_2O and H_2 both referred to gas phases. To convert the adsorption energy at zero temperature into the adsorption Gibbs free energy at the room temperature (T) and standard pressure (p^0), the electrode potential (U), entropy change (ΔS) and zero-point energy corrections (ΔZPE) to the adsorption energy together with the solvation correction ($\Delta G_{sol}+\Delta G_{PH}$) were considered. Herein, the change in Gibbs free energy (ΔG) for each reaction step of ORR could be given by the equation:

$$\Delta G = \Delta E + \Delta ZPE - T\Delta S + ne(U - U_0) + \Delta G_{sol} + \Delta G_{PH} \tag{15}$$

By setting the reference potential to be the standard hydrogen electrode, the free energy of $1/2H_2$ could be used to replace that of (OH⁻-e⁻). The free energy of O_2 was obtained from the reaction $2H_2O \rightarrow O_2+2H_2$ for which the free energy change is 4.92 eV. And a solvation correction with energy equals to -0.28 eV, +0.07 eV and -0.22 eV were applied to E_{HO*}, E_{O*} and E_{HOO*} respectively. Therefore, for ORR intermediates, the adsorption Gibbs free energies could be expressed as following:

$$\Delta G_{HOO*} = \Delta E_{HOO*} + \Delta ZPE - T\Delta S - 0.22 + 0.0591 \times PH - neU$$

$$\tag{16}$$

$$\Delta G_{HO*} = \Delta E_{HO*} + \Delta ZPE - T\Delta S - 0.28 + 0.0591 \times PH - neU \tag{17}$$

$$\Delta G_{O*} = \Delta E_{O*} + \Delta ZPE - T\Delta S + 0.07 + 0.0591 \times PH - neU \tag{18}$$

where, T was the room temperature (300K), entropy changes (ΔS) and zero point energies (ΔZPE) were employing as implemented in prior works and tabulated values.[8, 9]

Through the DFT calculation, we carefully calculated the relationship of the boron-doped with the d-band center with the equation:

$$E_{d-band\ center} = \frac{\int_{-\infty}^{E_F} E \cdot PDOS(E)dE}{\int_{-\infty}^{E_F} PDOS(E)dE} \tag{19}$$

5. *Aqueous zinc-air battery assembly:* All electrodes were directly used as the air cathodes, which were coated Fe_{SA}/B,N-CNT and Pt/C+IrO_2 on Nickel foam with the loading 3 mg cm^{-2}, and zinc plates were polished to be used as the anodes. Rechargeable aqueous zinc-air batteries were prepared with addition of 0.2 M $Zn(CH_3COO)_2$ into the 6 M KOH electrolyte.
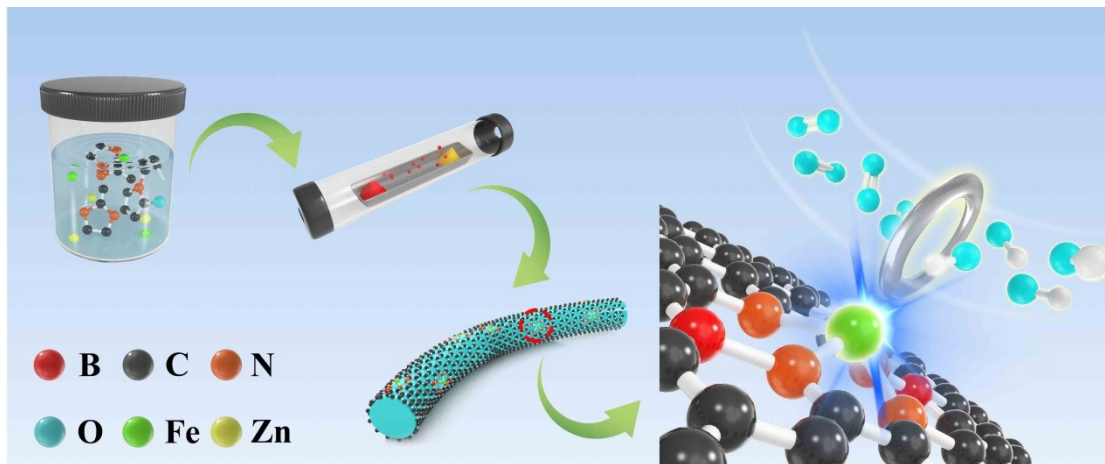
Fig. S1. Schematic procedure for the synthesis of Fe$_{SA}$/B,N-CNT.
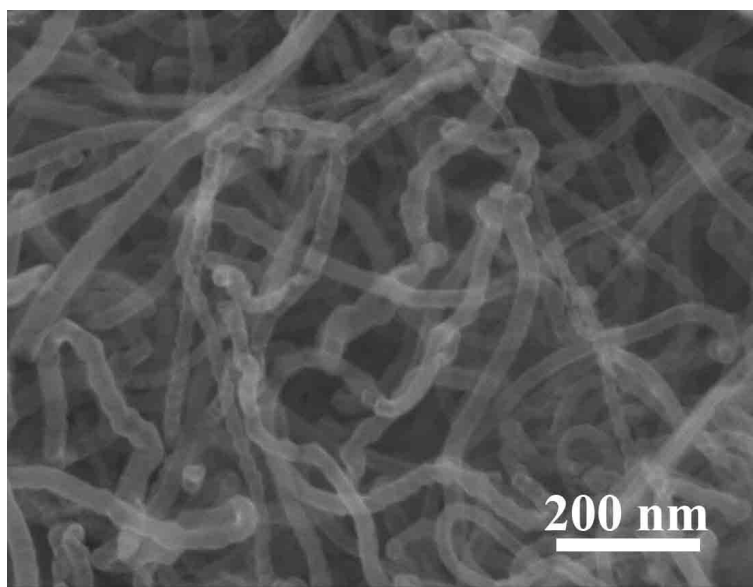
Fig. S2. SEM image of Fe$_{SA}$/B,N-CNT.
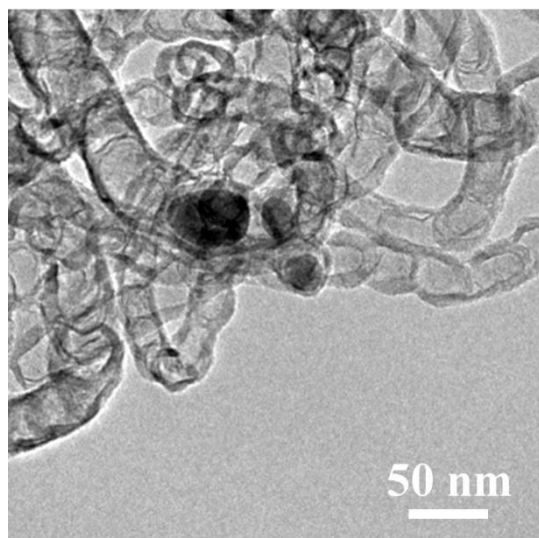
Fig. S3. TEM image of Fe_{NP}/N-CNT, in which iron-based particles are encapsulated either at the tip or inside of carbon nanotubes.
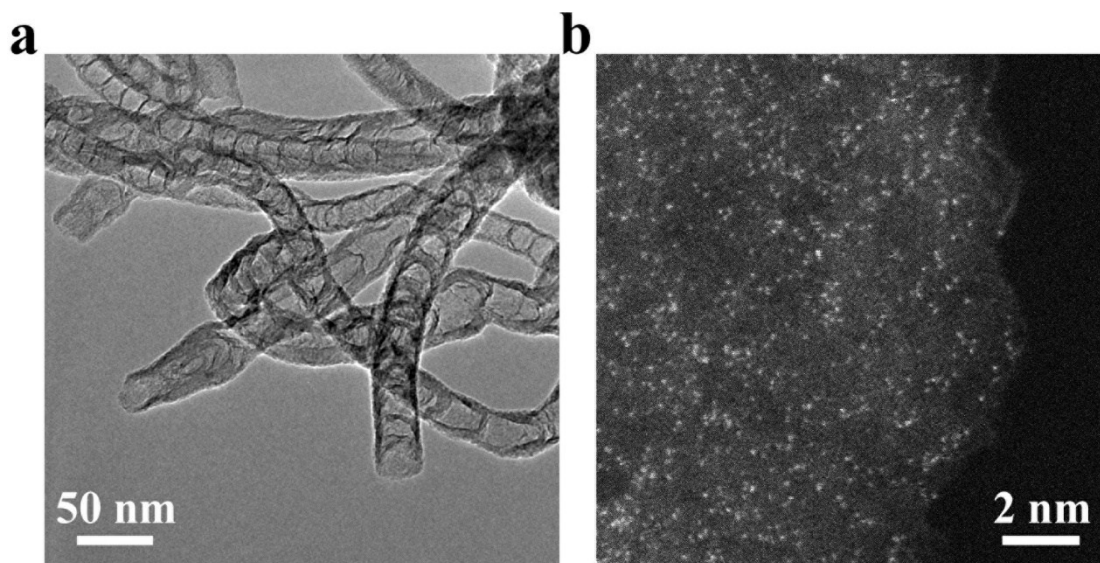
Fig. S4. TEM image and HAADF-STEM image of Fe$_{SA}$/N-CNT. Fe$_{SA}$/N-CNT exhibits the nanotube morphology without Fe aggregation. A large number of isolated bright dots representing single Fe atoms uniformly disperse on the carbon support.
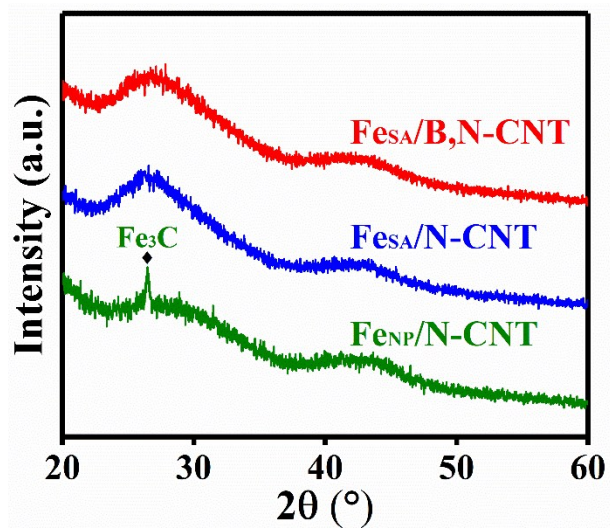
Fig. S5. XRD patterns of different samples. The results show no distinct differences between Fe$_{SA}$/B,N-CNT and Fe$_{SA}$/N-CNT, with two broad peaks assignable to the (002) and (101) planes of graphitic carbon. Notably, no peaks related to metallic Fe or other Fe species are observed. As for Fe$_{NP}$/N-CNT, it exhibits well-defined diffraction peaks associated with Fe-based carbides.
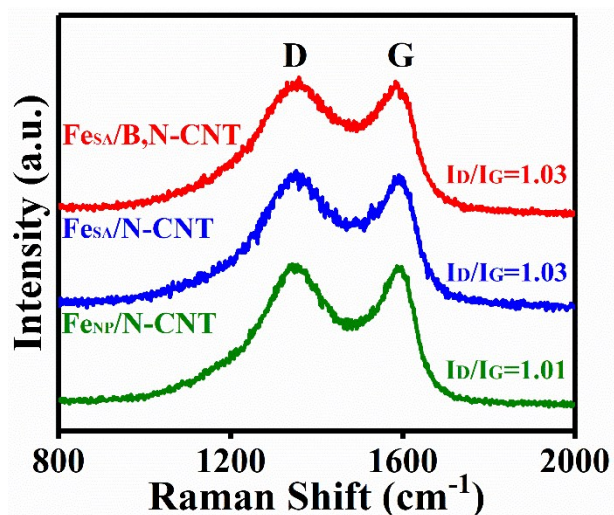
Fig. S6. Raman spectra of different samples. The D band (1360 cm^{-1}) and G band (1590 cm^{-1}) provide information on the disorder and crystallinity of carbon materials, respectively. Fe$_{NP}$/N-CNT shows the lowest I_D/I_G value of 1.01. As for catalysts with single-atom dispersed Fe, the I_D/I_G exhibits the same value of 1.03.
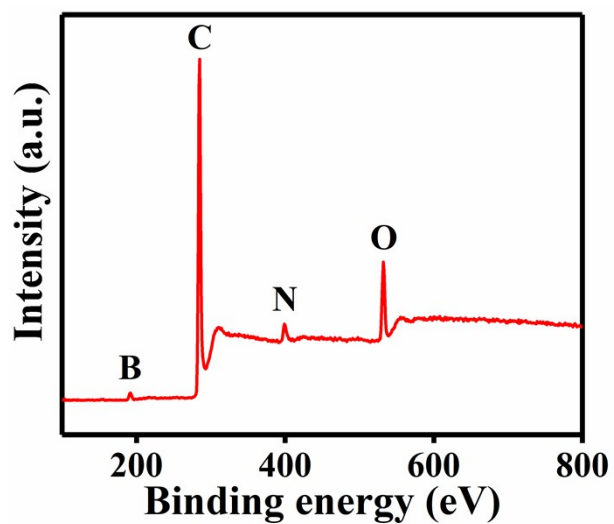
Fig. S7. XPS spectrum of Fe$_{SA}$/B,N-CNT. The survey scan indicates the presence of boron, carbon, nitrogen, and oxygen.
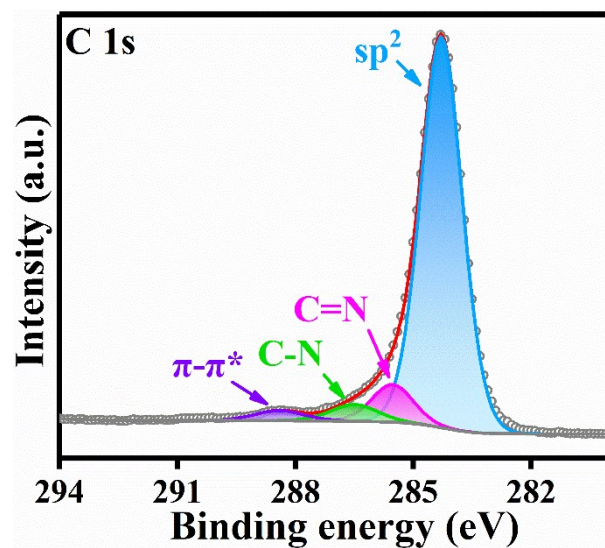
Fig. S8. High-resolution XPS spectra of C 1s of Fe_{SA}/B,N-CNT. Four forms of carbon are observed including sp^2 at ~284.3 eV, C=N at ~285.5 eV, C-N at ~286.5 eV, and π-π* at ~288.4 eV.
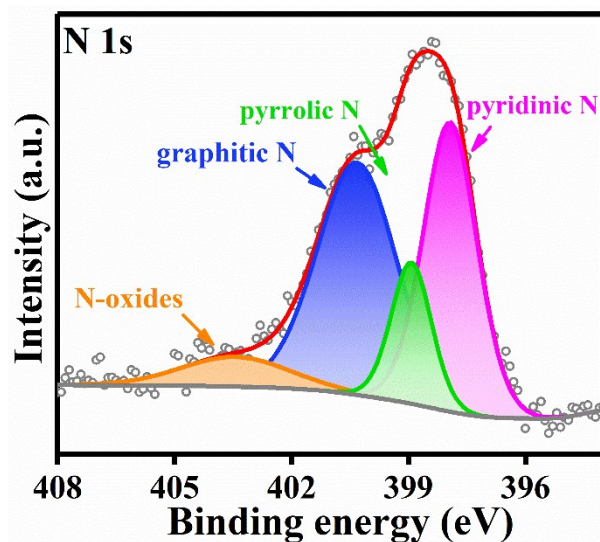
Fig. S9. High-resolution XPS spectrum of N 1s of Fe$_{SA}$/B,N-CNT. Four forms of nitrogen are observed including pyridinic N at ~398.1 eV, pyrrolic N at ~398.9 eV, graphitic N at ~400.4 eV, and N-oxides at ~403.6 eV.
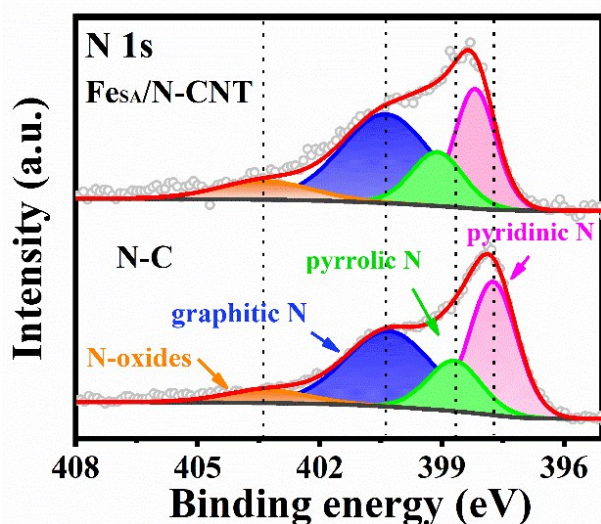
Fig. S10. High-resolution N 1s X-ray photoelectron spectra of the Fe_{SA}/N-CNT and N-C. The N 1s spectra of N-C were deconvoluted into four peaks, assignable to the pyridinic N (397.8 eV), pyrrolic N (398.7 eV), graphitic N (400.4 eV), and pyridine N-oxides (403.6 eV), respectively. Once Fe was present in the catalyst, both pyridinic N and pyrrolic N shifted to higher binding energy of 398.1 and 398.9 eV, respectively, while no discernible peak shift was observed in graphitic N or pyridine N-oxides. This suggest strong chemical bond forming between Fe and pyridinic/pyrrolic N with a high electronegativity, leading to partial electron migration from Fe to pyridinic/pyrrolic N.
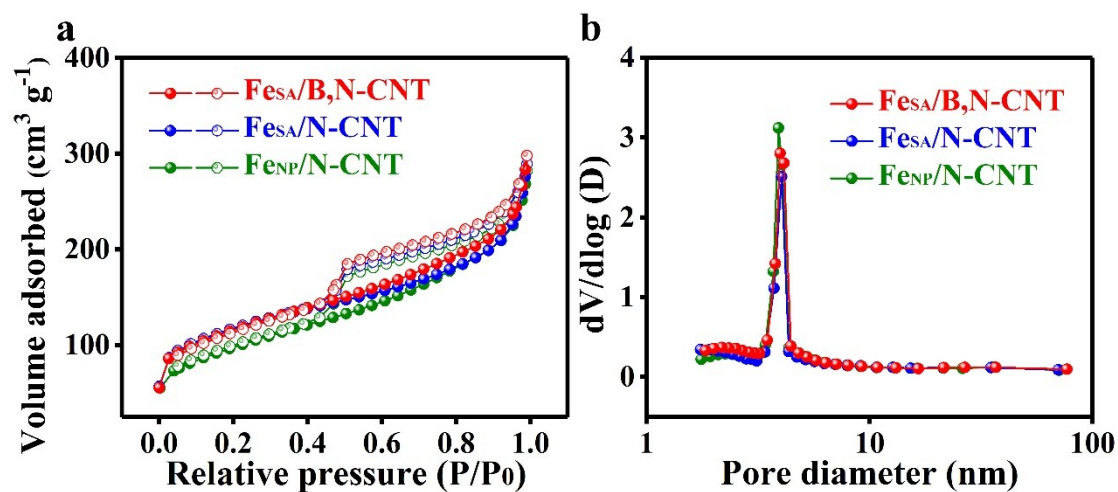
Fig. S11. (a) N_2 sorption isotherms and (b) pore size distribution curves of different samples. The specific surface area for each sample was calculated to be 399 m^2 g^{-1} for Fe_{SA}/B,N-CNT, 397 m^2 g^{-1} for Fe_{SA}/N-CNT, and 341 m^2 g^{-1} for Fe_{NP}/N-CNT. The typical mesopores centered at around 4 nm could facilitate the mass transfer during ORR process.
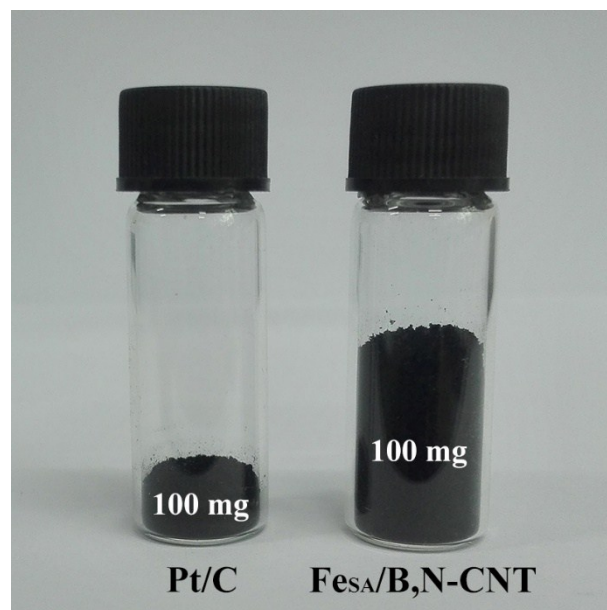
Fig. S12. Photographs of Fe$_{SA}$/B,N-CNT (100 mg, right) and commercial Pt/C (20 wt. % Pt, 100 mg, left) in vials. Fe$_{SA}$/B,N-CNT shows low volumetric density compared to commercial Pt/C catalyst.
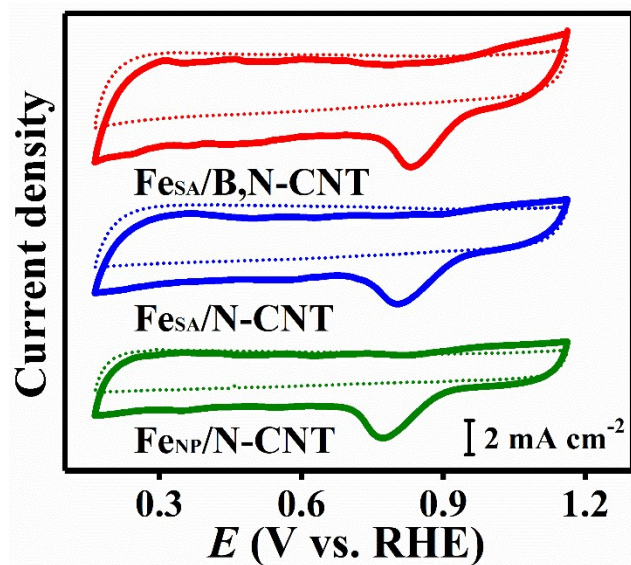
Fig. S13. CV curves of different samples in O_2-saturated (solid line) or N_2-saturated (dash line) 0.1 M KOH. No redox peak was observed when the solution was saturated with N_2. On the contrary, if the gas in the solution was replaced with O_2, an obvious onset potential was observed at ~1.06 V vs. RHE for Fe_{SA}/B,N-CNT, suggesting the superior ORR performance.
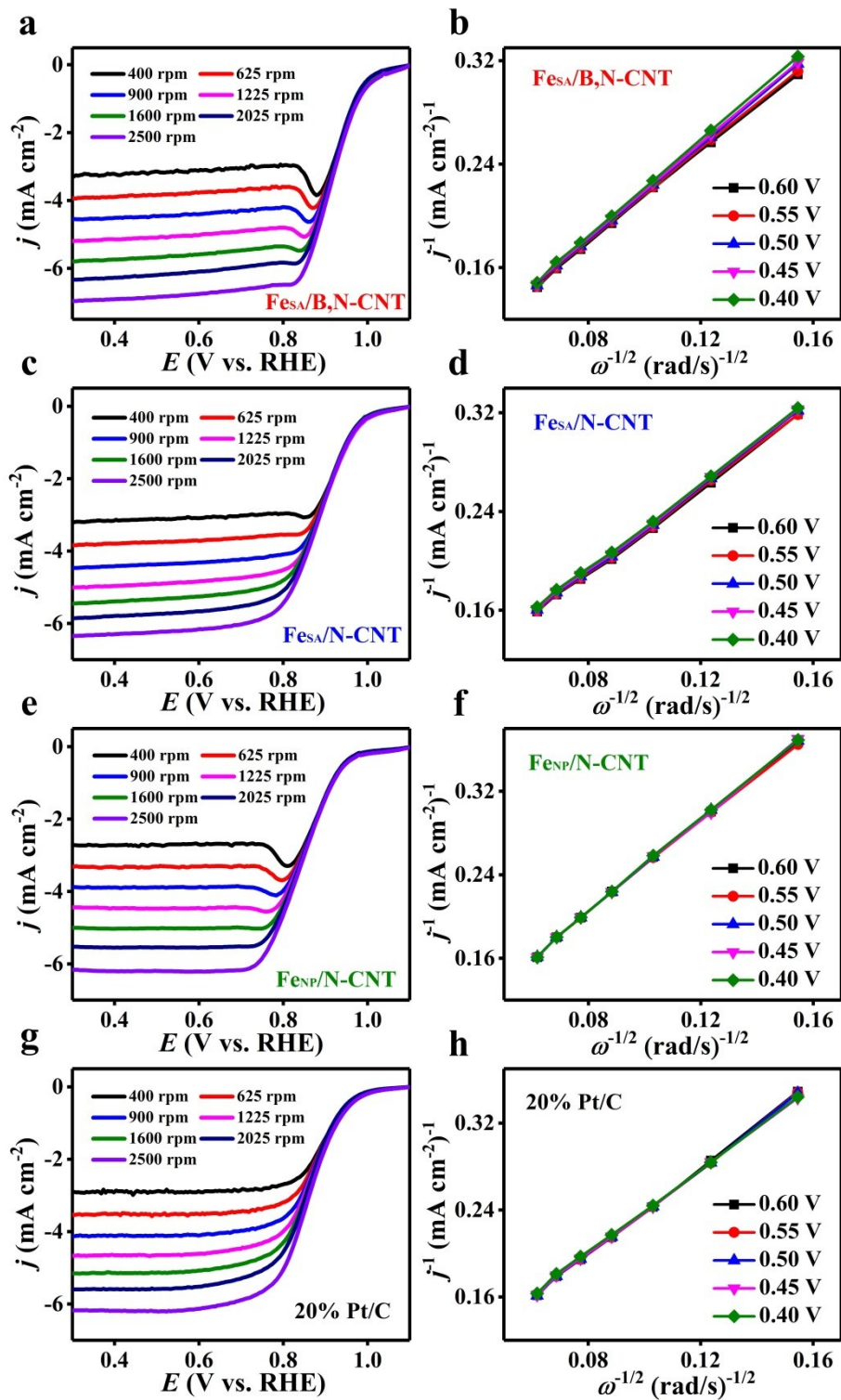
Fig. S14. LSV curves at different rotation speeds and the corresponding K-L plots at different potentials of (a,b) Fe$_{SA}$/B,N-CNT, (c,d) Fe$_{SA}$/N-CNT, (e,f) Fe$_{NP}$/N-CNT and (g,h) Pt/C.
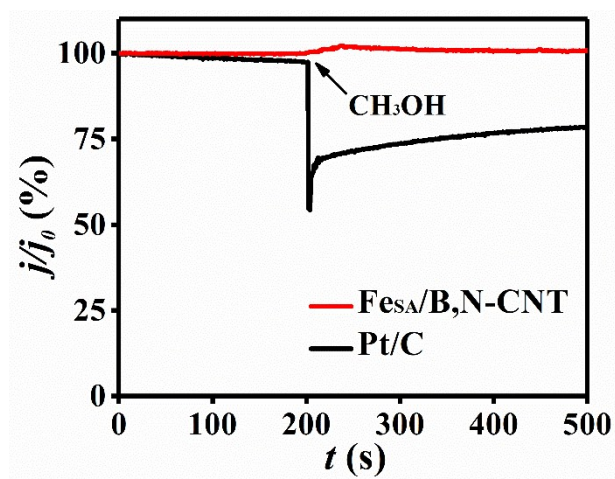
Fig. S15. Methanol resistance in O_2-saturated 0.1 M KOH tests without and with CH_3OH.
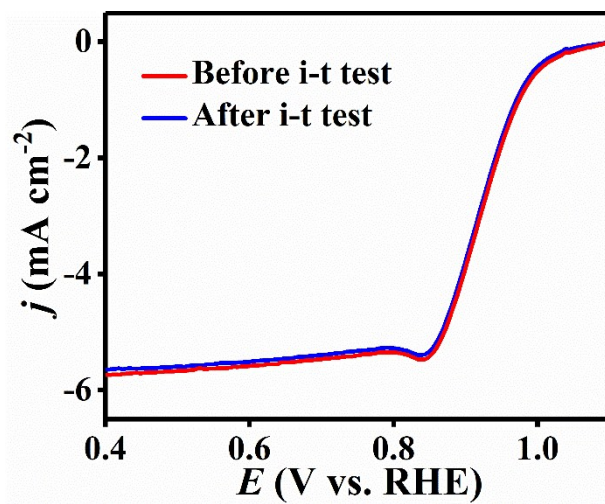
Fig. S16. ORR LSV curves of Fe$_{SA}$/B,N-CNT before and after 20000 s i-t test.
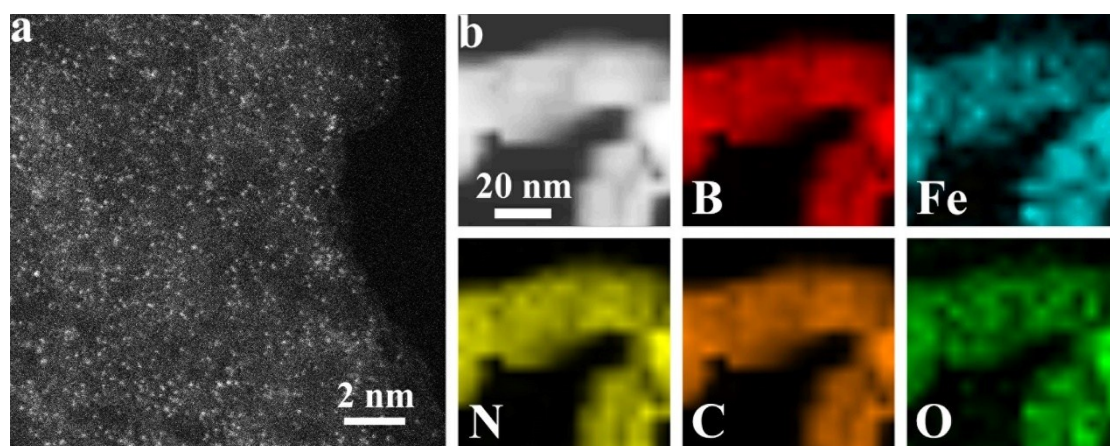
Fig. S17. (a) AC HAADF-STEM image and (b) HRTEM image and corresponding element mapping of Fe_{SA}/B,N-CNT after durability test, demonstrating the atomically dispersed Fe atoms remain unchanged.
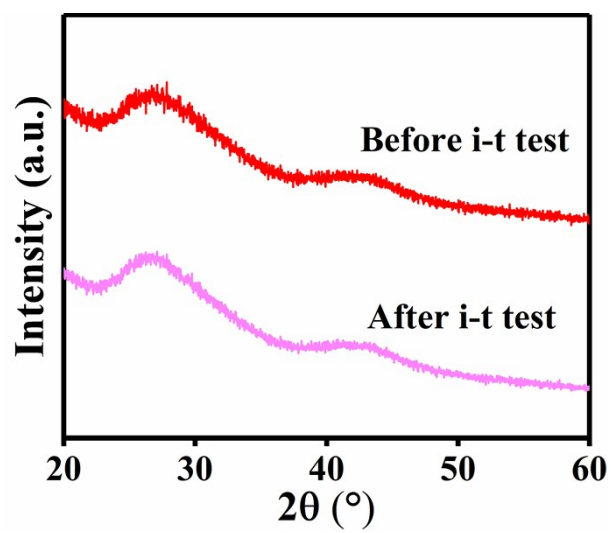
Fig. S18. XRD spectrum of the Fe_{SA}/B,N-CNT after test.
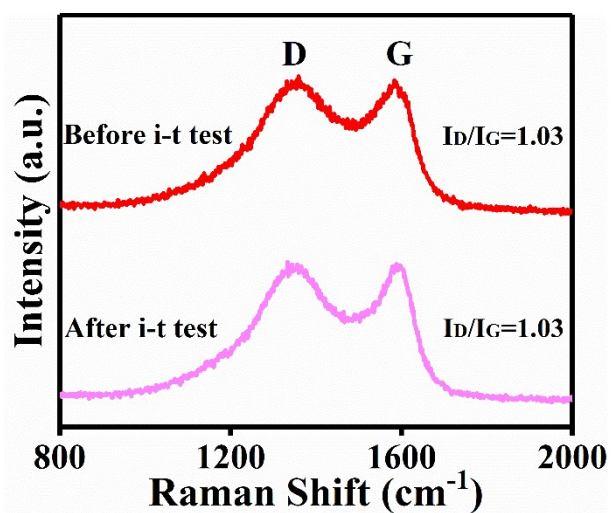
Fig. S19. Raman spectrum of the Fe_{SA}/B,N-CNT after durability test. I_D/I_G is the intensity ratio of the D peak to the G peak.
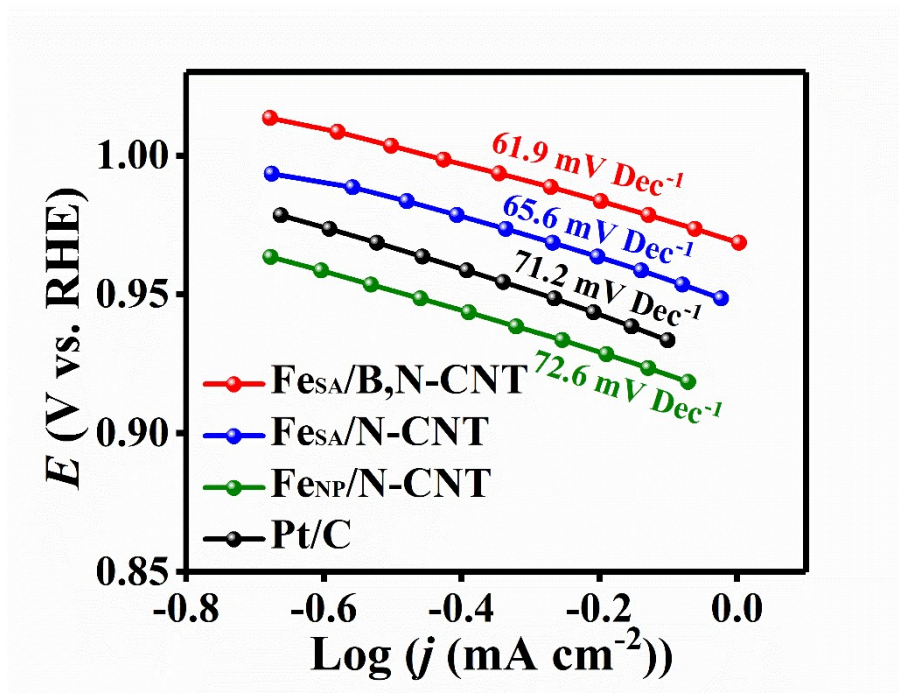
Fig. S20. ORR Tafel plots derived from the corresponding LSV curves. The much smaller Tafel slope of Fe$_{SA}$/B,N-CNT (61.9 mV/dec) compared to other samples indicates a more favorable reaction kinetics.
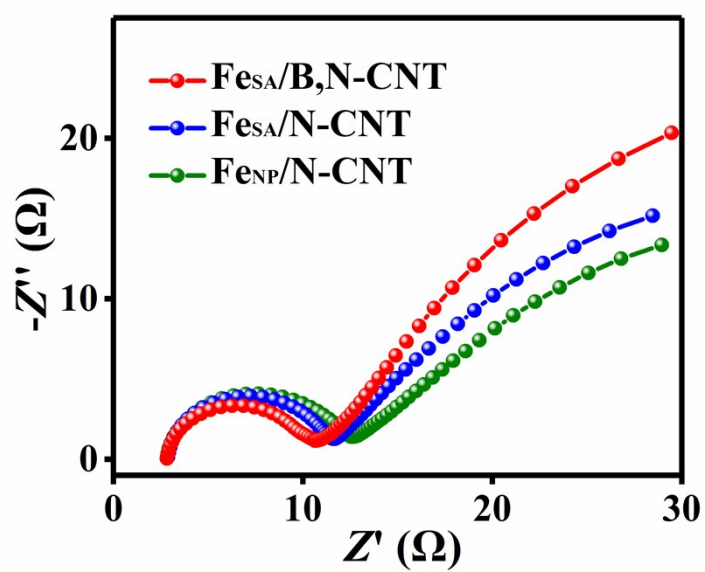
Fig. S21. EIS spectra of different samples. Fe_{SA}/B,N-CNT displays the smallest diameter of the semicircle and the largest slope among all the samples, confirming its fastest electron transport kinetics and ion diffusion rate.
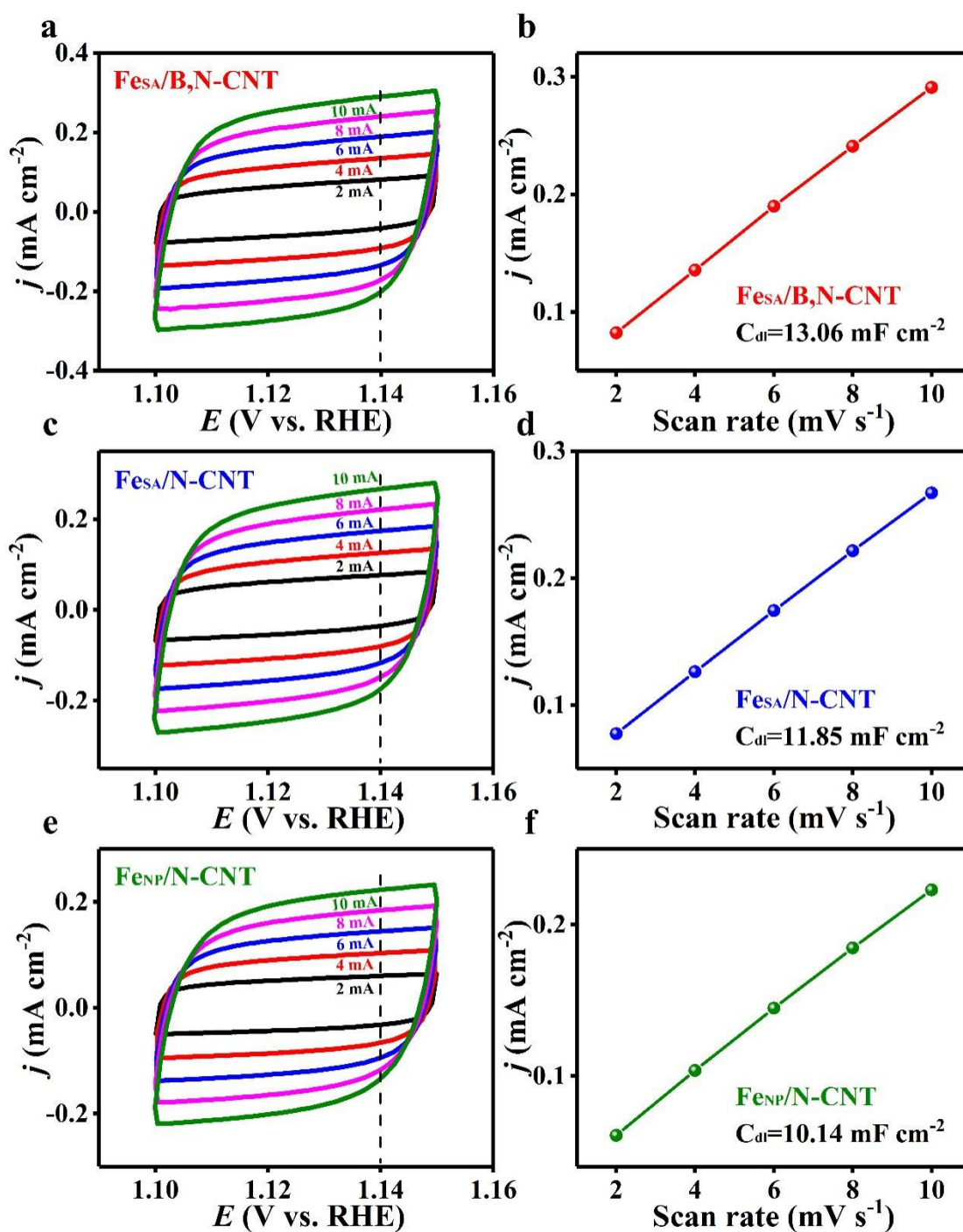
Fig. S22. Cyclic voltammetry curves of different samples in 2 M KCl solution and a plot of the current density at 1.14 V vs. the scan rate of (a,b) Fe_{SA}/B,N-CNT, (c,d) Fe_{SA}/N-CNT, and (e,f) Fe_{NP}/N-CNT. The double layer capacitance C_{dl} increases in the order of Fe_{NP}/N-CNT (10.14 mF cm^{-2}) < Fe_{SA}/N-CNT (11.85 mF cm^{-2}) < Fe_{SA}/B,N-CNT (13.06 mF cm^{-2}).
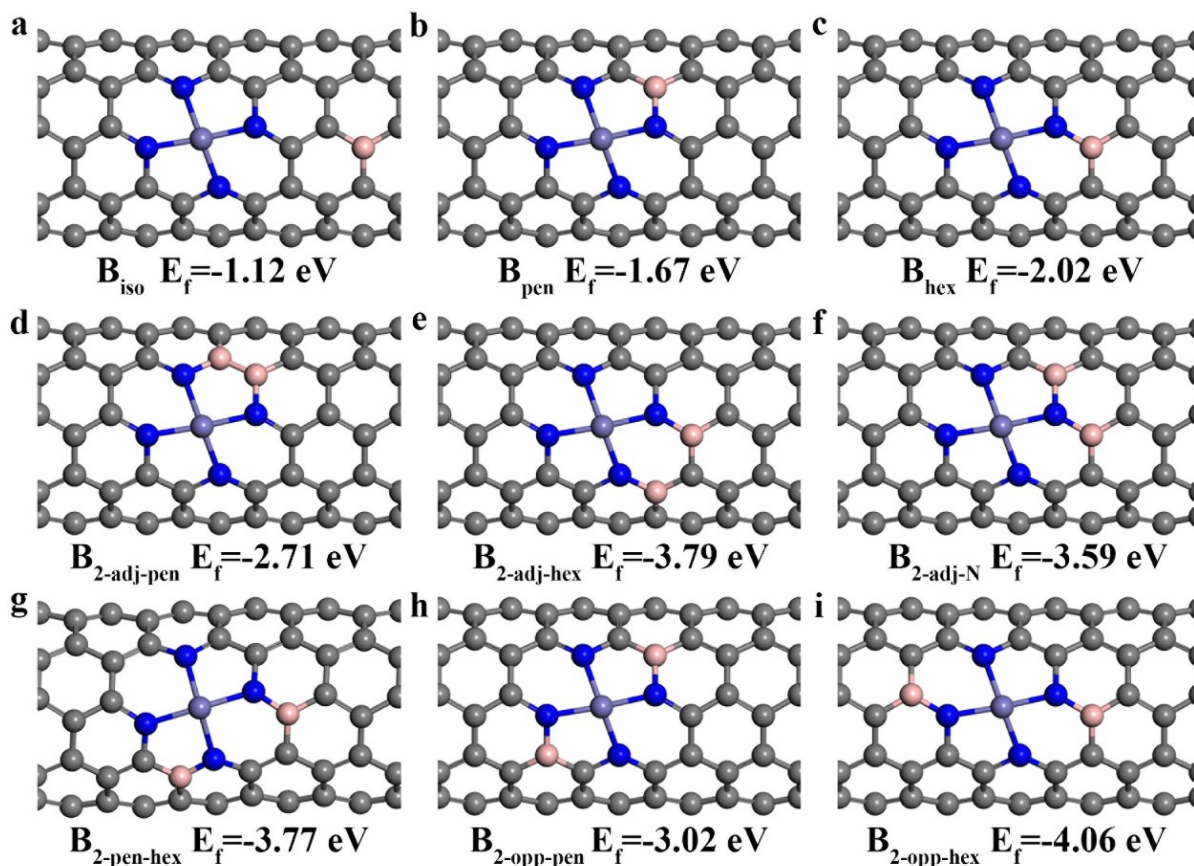
Fig. S23. The configurations and formation energies (E_f) of various possible B-doped FeN_4 active sites. A pentatomic ring consists of one Fe atom, two N atoms and two C atoms, the Fe and two N atoms together with three C atom compose a hexatomic ring. Purple, blue, pink, and grey represent Fe, N, B, and C atoms, respectively.
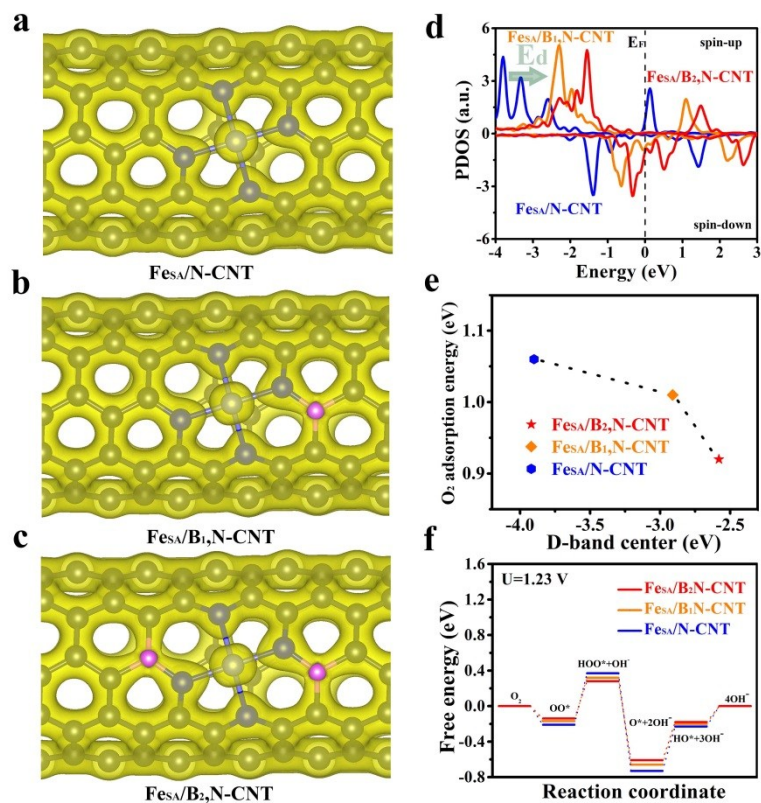
Fig. S24. The structure of (a) Fe$_{SA}$/N,CNT, (b) Fe$_{SA}$/B$_1$,N-CNT, and (c) Fe$_{SA}$/B$_2$,N-CNT. (d) The PDOS of Fe 3d band of the different catalysts. (e) The relation between d-band center and the O$_2$ adsorption of different catalysts. (f) The free energy of the catalysts at the equilibrium potential of U = 1.23 V.
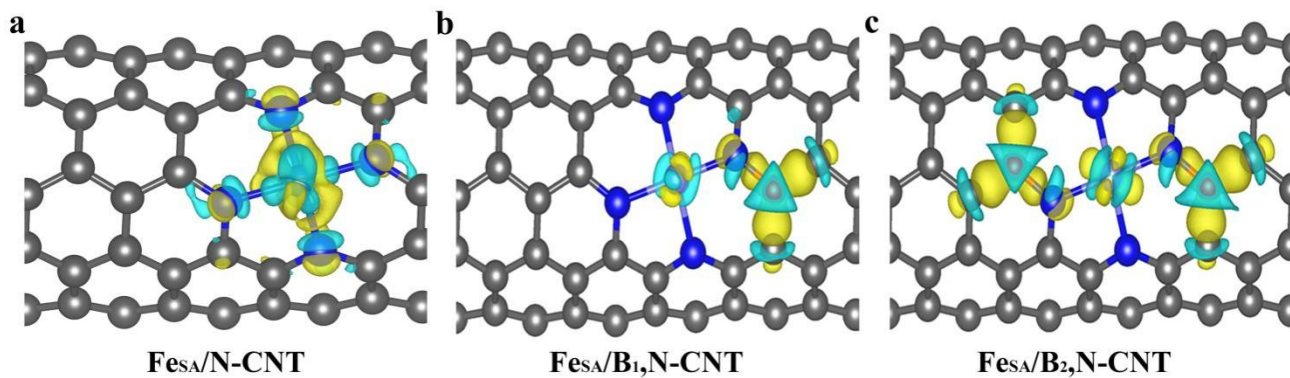
Fig. S25. The charge-density variation wave of the Fe_{SA}/N-CNT, Fe_{SA}/B_1,N-CNT and Fe_{SA}/B_2,N-CNT. Light blue area represented charge density decrease ($\Delta\rho < 0$) and yellow area denoted charge density increase ($\Delta\rho > 0$). Purple, blue, pink, and grey represent Fe, N, B, and C atoms, respectively.
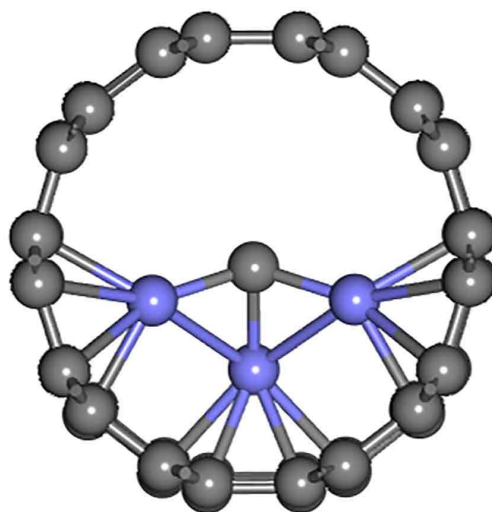
Fe_{NP}/N-CNT

Fig. S26. The optimized structure of Fe$_{NP}$/N-CNT. Purple, blue, and grey represent Fe, N, and C atoms, respectively.
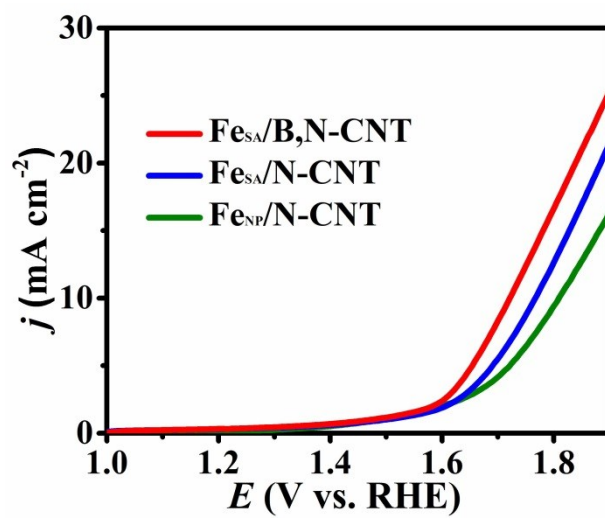
Fig. S27. Linear sweep voltammetry OER curves of Fe_{SA}/B,N-CNT, Fe_{SA}/N-CNT and Fe_{NP}/N-CNT.

6. Supplementary Tables

Table S1. Elemental compositions (C, O, N, and B) obtained by XPS spectroscopy, and Fe contents measured by ICP-OES.

	C(at%)	O(at%)	N(at%)	B(at%)	Fe(at%)
$Fe_{SA}/B,N$-CNT	85.55	6.99	3.68	3.68	0.10
Fe_{SA}/N-CNT	90.06	5.92	3.86	NA	0.16
Fe_{NP}/N-CNT	88.88	6.68	3.99	NA	0.44

Table S2. Comparison of ORR activity of various non-precious metal catalysts in 0.1 M KOH.

Catalyst	E_{onset} vs. RHE (V)	$E_{1/2}$ vs. RHE(V)	$J_k|_{V=0.85\ V}$ (mA cm^{-2})	K_{tafel} (mV dec^{-1})	Ref.
$Fe_{SA}/B,N$-CNT	1.07	0.933	62.57	61.9	This work
Fe_{SA}/N-CNT	1.04	0.890	13.17	65.6	This work
Fe-ISAs/CN	0.986	0.900	37.85	58	10
SA-Fe-HPC	/	0.890	3.72	49	11
$FeCl_1N_4/CNS$	/	0.921	41.11	51	12
N-GCNT/FeCo	1.03	0.920	/	66.8	13

Fe-ISA/SNC	/	0.896	100.7	44	14
Fe-N$_4$ SAs/NPC	0.972	0.885	/	91	15
Fe$_{SA}$-N-C	/	0.891	23.27	/	16
FeCo-ISAs/CN	0.995	0.920	31.1$|_{0.88\,V}$	57	17
Fe$_3$C-Fe,N/C-900	/	0.881	/	/	18
BCN-FNHs	0.886	0.861	/	91.2	19
Fe-N/C-800	0.98	0.81	/	59	20
CNT/PC	/	0.88	2.4$|_{0.9\,V}$	/	21
Fe@C-FeNC-2	1.00	0.899	/	68	22
CNT/HDC-1000	0.92	0.82	8.3$|_{0.8\,V}$	65.1	23
FePhen@MOFArNH$_3$	1.03	0.86	/	/	24
NCNTFs	/	0.87	/	64	25
BN-GQD/G-30	/	0.7	11.1	/	26
pCNT@Fe$_{1.5}$@GL	/	0.867	/	65.2	27
NCMT-1000 (3D)	1.05	0.89	/	/	28
FePc–Py–CNTs	/	0.915	/	27	29

FeN$_x$/C-700-20	1.1	0.9	/	93	30
Fe−N−CC	0.94	0.83	18.3|$_{0.58 V}$	/	31
Fe-NMCSs	1.027	0.86	/	/	32
FeSAs/PTF-600	1.01	0.87	/	62	33
Fe/N/G-0.25	0.98	0.84	/	90	34
Fe$_3$C/NCNTs/OBP-900	1.00	0.89	/	74.3	35
BNG-2.5-1000	1.01	0.816	26.62	/	36
IL-1-C	0.96	0.87	/	60	37
Fe$_{15}$−N−C1000	0.99	0.85	/	62	38
FePPyC-900	0.96	0.877	/	95	39
Fe/Fe$_3$C@N−C−NaCl	0.97	0.869	/	67	40
Fe-N/C-1/30	1.04	0.895	/	/	41
Meso/micro-PoPD	/	0.85	4.23|$_{0.8 V}$	/	42
CNPs	1.03	0.92	/	/	43
Fe$_3$C@N-CNT	0.95	0.85	/	78	44
COP-TPP(Fe)@MOF-900	0.99	0.846	/	68	45

SA-Fe/NG	/	0.88	10	82	46
FeNC-20-1000	1.04	0.88	/	49	47
N-Fe-MOF	1.05	0.88	/	/	48
SA-Fe-N-1.5-800	/	0.910	/	62	49
25% Cu-N/C	0.917	0.813	$35.2|_{0.75\,V}$	45.8	50
Co SAs/N-C(900)	/	0.881	$22|_{0.8\,V}$	75	51
Co–N$_x$/C NRA	/	0.877	/	66	52
NC@Co-NGC DSNC	/	0.82	$12.8|_{0.71\,V}$	51	53
ZIF-TAA-p	0.98	0.88	/	/	54
C-CZ-4-1000	1.03	0.887	/	49	55
Co@MCM	0.95	0.86	/	96	56
Co-ISAS/p-CN	/	0.838	$5.1|_{0.83\,V}$	61	57
CuCo@NC	0.96	0.884	/	80	58

Table S3. Free energy change (ΔG) for the 4-electron transfer processes during ORR at T = 298 K, PH = 13 and U = 0 V.

Elementary steps	ΔG		
	Fe_{NP}/CNT	Fe_{SA}/N-CNT	Fe_{SA}/B,N-CNT
$* + O_2 \rightarrow OO*$	5.22	4.71	4.78
$OO* + H_2O + e^- \rightarrow HOO* + OH^-$	4.85	4.06	3.97
$HOO* + e^- \rightarrow O* + OH^-$	2.50	1.73	1.85
$O* + H_2O + e^- \rightarrow HO* + OH^-$	1.68	1.00	1.05
$HO* + e^- \rightarrow * + OH^-$	0.00	0.00	0.00

References

1 V. Blum, R. Gehrke, F. Hanke, P. Havu, V. Havu, X. Ren, K. Reuter and M. Scheffler, *Comput. Phys. Commun.*, 2009, **180**, 2175-2196.

2 J. P. Perdew, K. Burke and M. Ernzerhof, *Phys. Rev. Lett.*, 1998, **77**, 3865-3868.

3 G. Kresse and D. Joubert, *Phys. Rev. B*, 1999, **59**, 1758-1775.

4 H. J. Monkhorst and J. D. Pack, *Phys. Rev. B*, 1976, **13**, 5188-5192.

5 A. Tkatchenko and M. Scheffler, *Phys. Rev. Lett.*, 2009, **102**, 073005.

6 V. G. Ruiz, W. Liu, E. Zojer, M. Scheffler and A. Tkatchenko, *Phys. Rev. Lett.*, 2012, **108**, 146103.

7 C. Freysoldt, B. Grabowski, T. Hickel, J. Neugebauer, G. Kresse, A. Janotti and C. G. V. D. Walle, *Rev. Mod. Phys.*, 2014, **86**, 253-305.

8 G. S. Karlberg, J. Rossmeisl and J. K. Nørskov, *Phys. Chem. Chem. Phys.*, 2007, **9**, 5158-5161.

9 A. Holewinski, J. C. Idrobo and S. Linic, *Nat. Chem.*, 2014, **6**, 828-834.

10 Y. Chen, S. Ji, Y. Wang, J. Dong, W. Chen, Z. Li, R. Shen, L. Zheng, Z. Zhuang and D. Wang, *Angew. Chem. Int. Ed.*, 2017, **129**, 6937-6941.

11 Z. P. Zhang, J. T. Sun, F. Wang and L. M. Dai, *Angew. Chem. Int. Ed.*, 2018, **57**, 9038-9043.

12 Y. H. Han, Y. G. Wang, R. R. Xu, W. X. Chen and Y. D. Li, *Energy Environ. Sci.*, 2018, **11**, 2348-2352.

13 S. Li, C. Cheng, X. Zhao, J. Schmidt and A. Thomas, *Angew. Chem. Int. Ed.*, 2018, **57**, 1856.

14 Q. Li, W. Chen, H. Xiao, Y. Gong, Z. Li, L. Zheng, X. Zheng, W. Yan, W. C. Cheong and R. Shen, *Adv. Mater.*, 2018, **30**, 1800588.

15 Y. Pan, S. Liu, K. Sun, X. Chen, B. Wang, K. Wu, X. Cao, W. C. Cheong, R. Shen and A. Han, *Angew. Chem. Int. Ed.*, 2018, **57**, 8614-8618.

16 H. L. Jiang, L. Jiao, G. Wan, R. Zhang, H. Zhou and S. H. Yu, *Angew. Chem. Int. Ed.*, 2018, **57**, 8525-8529.

17 D. Zhang, W. Chen, Z. Li, Y. Chen, L. Zheng, Y. Gong, Q. Li, R. Shen, Y. Han and W. C. Cheong, *Chem. Commun.*, 2018, **54**, 4274-4277.

18 H. Tan, Y. Li and J. Kim, *Adv. Sci.*, 2018, **5**, 1800120.

19 Y. Wenxiu, L. Xiangjian, Y. Xiaoyu, J. Jianbo and G. Shaojun, *J. Am. Chem. Soc.*, 2015, **137**, 1436.

20 W. H. Niu, L. G. Li, X. J. Liu, N. Wang, J. Liu, W. J. Zhou, Z. H. Tang and S. W. Chen, *J. Am. Chem. Soc.*, 2015, **137**, 5555-5562.

21 Y. J. Sa, D. J. Seo, J. Woo, J. T. Lim, J. Y. Cheon, S. Y. Yang, J. M. Lee, D. Kang, T. J. Shin and H. S. Shin, *J. Am. Chem. Soc.*, 2016, **138**, 15046-15056.

22 W. J. Jiang, L. Gu, L. Li, Y. Zhang, X. Zhang, L. J. Zhang, J. Q. Wang, J. S. Hu, Z. D. Wei and L. J. Wan, *J. Am. Chem. Soc.*, 2016, **138**, 3570-3578.

23 Y. J. Sa, C. Park, Y. J. Hu, S. H. Park, G. G. Park and H. J. Sang, *Angew. Chem.*, 2015, **126**, 4186-4190.

24 K. Strickland, E. Miner, Q. Jia, U. Tylus, N. Ramaswamy, W. Liang, M. T. Sougrati, F. Jaouen and S. Mukerjee, *Nat. Commun.*, 2015, **6**, 7343.

25 B. Y. Xia, Y. Yan, N. Li, H. B. Wu, X. W. Lou and X. Wang, *Nat. Energy*, 2016, **1**, 15006.

26 H. L. Fei, R. Q. Ye, G. L. Ye, Y. J. Gong, Z. W. Peng, X. J. Fan, E. L. G. Samuel, P. M. Ajayan and J. M. Tour, *Acs Nano*, 2014, **8**, 10837-10843.

27 S. H. Ahn, X. Yu and A. Manthiram, *Adv. Mater.*, 2017, **29**, 1606534.

28 J. C. Li, P. X. Hou, S. Y. Zhao, C. Liu, D. M. Tang, M. Cheng, F. Zhang and H. M. Cheng, *Energy Environ. Sci.*, 2016, **9**, 3079-3084.

29 R. Cao, R. Thapa, H. Kim, X. Xu, G. K. Min, Q. Li, N. Park, M. Liu and J. Cho, *Nat. Commun.*, 2012, **4**, 2076.

30 S. C. Han, X. Y. Hu, J. C. Wang, X. S. Fang and Y. F. Zhu, *Adv. Energy Mater.*, 2018, **8**, 1800955.

31 G. A. Ferrero, K. Preuss, A. Marinovic, A. B. Jorge, N. Mansor, D. J. Brett, A. B. Fuertes, M. Sevilla and M. M. Titirici, *Acs Nano*, 2016, **10**, 5922-5932.

32 F. L. Meng, Z. L. Wang, H. X. Zhong, J. Wang, J. M. Yan and X. B. Zhang, *Adv. Mater.*, 2016, **28**, 7948-7955.

33 J. D. Yi, R. Xu, Q. Wu, T. Zhang, K. T. Zang, J. Luo, Y. L. Liang, Y. B. Huang and R. Cao, *ACS Energy Lett.*, 2018, **3**, 883-889.

34 C. Dominguez, F. J. Pérez-Alonso, M. A. Salam, S. A. AlThabaiti, M. A. Peña, L. Barrio and S. Rojas, *J. Mater. Chem. A*, 2015, **3**, 24487-24494.

35 J. Zhu, M. Xiao, C. Liu, J. Ge, J. St-Pierre and X. Wei, *J. Mater. Chem. A*, 2015, **3**, 21451-21459.

36 J. T. Jin, F. P. Pan, L. H. Jiang, X. G. Fu, A. M. Liang, Z. Y. Wei, J. Y. Zhang and G. Q. Sun, *Acs Nano*, 2014, **8**, 3313-3321.

37 H. Fei, X. Chen, Y. Shen, L. Ying, A. Liu, S. Liu, T. Mori and Y. Zhang, *J. Mater. Chem. A*, 2016, **4**, 6630-6638.

38 Y. Qian, D. Pan, P. Wu, C. Cai and D. F. Gervasio, *J. Phys. Chem. C*, 2016, **120**, 9884-9896.

39 T. N. Tran, K. P. Singh, M. Y. Song, D. S. Yang and J. S. Yu, *J. Mater. Chem. A*, 2016, **4**, 8645-8657.

40 Y. Zhang, L. B. Huang, W. Jiang, X. Zhang, Y. Y. Chen, Z. Wei, L. J. Wan and J. S. Hu, *J. Mater. Chem. A*, 2016, **4**, 7781-7787.

41 W. Wei, X. M. Shi, P. Gao, S. S. Wang, W. Hu, X. X. Zhao, Y. M. Ni, X. Y. Xu, Y. Q. Xu, W. S. Yan, H. X. Ji and M. H. Cao, *Nano Energy*, 2018, **52**, 29-37.

42 H. W. Liang, X. Zhuang, S. Brüller, X. Feng and K. Müllen, *Nat. Commun.*, 2014, **5**, 4973.

43 S. L. Zhao, H. J. Yin, L. Du, L. C. He, K. Zhao, L. Chang, G. P. Yin, H. J. Zhao, S. Q. Liu and Z. Y. Tang, *ACS Nano*, 2014, **8**, 12660-12668.

44 B. Guan, L. E. Yu and X. W. Lou, *Energy Environ. Sci.*, 2016, **9**, 3092-3096.

45 J. Guo, Y. Li, Y. Cheng, L. Dai and Z. Xiang, *Acs Nano*, 2017, **11**, 8379-8386.

46 L. Yang, D. J. Cheng, H. X. Xu, X. F. Zeng, X. Wan, J. L. Shui, Z. H. Xiang and D. P. Cao, *P. Natl. Acad. Sci. USA*, 2018, **115**, 6626-6631.

47 T. Liu, P. P. Zhao, X. Hua, W. Luo, S. L. Chen and G. Z. Cheng, *J. Mater. Chem. A*, 2016, **4**, 11357-11364.

48 Q. Li, P. Xu, W. Gao, S. G. Ma, G. Q. Zhang, R. G. Cao, J. Cho, H. L. Wang and G. Wu, *Adv. Mater.*, 2014, **26**, 1378-1386.

49 Z. P. Miao, X. M. Wang, M. C. Tsai, Q. Q. Jin, J. S. Liang, F. Ma, T. Y. Wang, S. J. Zheng, B. J. Hwang, Y. H. Huang, S. J. Guo and Q. Li, *Adv. Energy Mater.*, 2018, **8**, 1801226.

50 Q. X. Lai, J. J. Zhu, Y. X. Zhao, Y. Y. Liang, J. P. He and J. H. Chen, *Small* 2017, **13**, 1700740.

51 P. Yin, T. Yao, Y. Wu, L. Zheng, Y. Lin, W. Liu, H. Ju, J. Zhu, X. Hong and Z. Deng, *Angew. Chem. Int. Ed.*, 2016, **55**, 10958-10963.

52 I. S. Amiinu, X. B. Liu, Z. H. Pu, W. Q. Li, Q. D. Li, J. Zhang, H. L. Tang, H. N. Zhang and S. C. Mu, *Adv. Funct. Mater.*, 2018, **28**, 1704638.

53 S. Liu, Z. Wang, S. Zhou, F. Yu, M. Yu, C. Y. Chiang, W. Zhou, J. Zhao and J. Qiu, *Adv. Mater.*, 2017, **29**, 1700874.

54 C. Zhang, B. An, L. Yang, B. Wu, W. Shi, Y. C. Wang, L. S. Long, C. Wang and W. B. Lin, *J. Mater. Chem. A*, 2016, **4**, 4457-4463.

55 L. Ge, Y. Yang, L. Wang, W. Zhou, R. De Marco, Z. Chen, J. Zou and Z. Zhu, *Carbon*, 2015, **82**, 417-424.

56 H. Zhang, Z. Wei, C. Tao, B. Guan and X. W. Lou, *Energy Environ. Sci.*, 2018, **11**, 1980-1984.

57 A. J. Han, W. X. Chen, S. L. Zhang, M. L. Zhang, Y. H. Han, J. Zhang, S. F. Ji, L. R. Zheng, Y. Wang, L. Gu, C. Chen, Q. Peng, D. s. Wang and Y. d. Li, *Adv. Mater.*, 2018, **30**, 1706508.

58 Y. L. Liu, F. J. Chen, Y. Wen, Z. Min, H. Na, F. P. Zhao, X. X. Wang and Y. G. Li, *Adv. Funct. Mater.*, 2017, **27**, 1606034.